

Structural phase transitions and superconductivity in the Heusler intermetallics XPd_2Sn ($X = Ti, Zr, Hf$)

Hang Su,^{1,2} Feng Du,^{1,2} Rui Li,^{1,2} Shuaishuai Luo,^{1,2} Yuxuan Chen,³ Jiyong Liu,⁴ Ye Chen,^{1,2} Chao Cao,¹ Michael Smidman,^{1,2,*} and Huiqiu Yuan^{1,2,5,6,†}

¹Center for Correlated Matter and Department of Physics, Zhejiang University, Hangzhou 310058, China

²Zhejiang Province Key Laboratory of Quantum Technology and Device,
Department of Physics, Zhejiang University, Hangzhou 310058, China

³Hangzhou Xuejun High School, Hangzhou 310012, China

⁴Department of Chemistry, Zhejiang University, Hangzhou 310027, China

⁵State Key Laboratory of Silicon Materials, Zhejiang University, Hangzhou 310058, China

⁶Collaborative Innovation Center of Advanced Microstructures, Nanjing University, Nanjing, 210093, China

(Dated: March 7, 2023)

We report the discovery of structural phase transitions and superconductivity in the full Heusler compounds XPd_2Sn ($X = Ti, Zr, Hf$), by means of electrical transport, magnetic susceptibility, specific heat and x-ray diffraction measurements. $TiPd_2Sn$, $ZrPd_2Sn$ and $HfPd_2Sn$ undergo structural phase transitions from the room-temperature cubic $MnCu_2Al$ -type structure (space group $Fm\bar{3}m$) to a low-temperature tetragonal structure at around 160 K, 110 K and 90 K, respectively, which are likely related charge density wave (CDW) instabilities. Low temperature single crystal x-ray diffraction measurements of $ZrPd_2Sn$ demonstrate the emergence of a superstructure with multiple commensurate modulations below T_s . $ZrPd_2Sn$ and $HfPd_2Sn$ have bulk superconductivity (SC) with transition temperatures $T_c \sim 1.2$ K and 1.3 K, respectively. Density functional theory (DFT) calculations reveal evidence for structural and electronic instabilities which can give rise to CDW formation, suggesting that these XPd_2Sn systems are good candidates for examining the interplay between CDW and SC.

I. INTRODUCTION

Since the discovery of the prototype compound $MnCu_2Al$ by Heusler in 1903, a large number of Heusler intermetallic materials have been reported with the formula AT_2M [1–3], where A is an early transition metal or small rare earth, T is a late transition metal and M is an electronegative p-block element. Most Heusler compounds have a cubic structure and a wide variety of physical properties and ground states have been reported, including heavy fermion behavior [4, 5], shape memory effects [6], topologically nontrivial states [7] and half-metallic ferromagnetism [8–10]. Due to the large number of members in this family, many of the properties can be tuned by chemical substitution [11–13]. In addition, a tetragonal crystal structure has been observed in a few Heusler compounds [e.g. TRh_2Sn ($T = V, Cr, Fe, Co$)], which corresponds to a distortion of the typical cubic structure [14]. Superconductivity (SC) has also been reported in Heusler materials, mostly in compounds containing Pd, Ni, or Au at the T site and the highest observed transition temperature T_c is currently 4.9 K (YPd_2Sn) [15]. In addition, the coexistence of superconductivity (SC) and long range magnetic order has been observed in $YbPd_2Sn$ and $ErPd_2Sn$ [16]. The valence electron count (VEC) has been found to be closely related to the superconducting properties, where the maximum values of T_c are at around $VEC = 27$ [17].

Charge density wave (CDW) order corresponds to an instability in the electronic states near the Fermi level,

where there is a periodic modulation of the electronic charge below the transition temperature due to the opening of a gap, which is usually concomitant with a structural phase transition [18, 19]. The coexistence of CDW and SC has been reported in some systems and the interplay between these orders has been of great interest [20–29]. The Heusler compound $LuPt_2In$ was recently reported to exhibit a second-order CDW transition at $T_{CDW} = 490$ K, as well as superconductivity below $T_c = 0.45$ K. Substituting Pd for Pt suppresses T_{CDW} to zero giving rise to a possible quantum critical point (QCP). T_c was also strongly enhanced as the CDW is suppressed, giving rise to a new scenario for the interplay between CDW and SC [30]. On the other hand besides $LuPt_2In$, structural distortions are also reported in $YbPt_2In$ [31] and $REAu_2In$ ($RE = La-Nd$) [32], but the coexistence of CDW/structural phase transitions and SC is not commonly observed in Heusler materials. It is therefore of particular interest to identify additional Heusler compounds exhibiting both CDW order and superconductivity, in order to examine the relationship between these competing orders, determine the origin of the CDW instabilities and to search for potential CDW QCP's.

In this article, we report the discovery of structural phase transitions and superconductivity in the Heusler compounds XPd_2Sn ($X = Ti, Zr, Hf$). Electrical resistivity, specific heat, magnetic susceptibility and x-ray diffraction measurements indicate that $TiPd_2Sn$, $ZrPd_2Sn$ and $HfPd_2Sn$ undergo CDW-like structural phase transitions from the cubic $MnCu_2Al$ type phase to a tetragonal structure upon cooling across $T_s \sim 160$ K,

110 K and 90 K, respectively. The structural instabilities are also revealed by DFT calculations of the imaginary phonon modes. At lower temperatures, ZrPd_2Sn and HfPd_2Sn undergo superconducting transitions at $T_c \sim 1.2$ K and 1.3 K, respectively. These findings suggest that XPd_2Sn are good candidates for investigating the interplay of CDW order and SC.

II. EXPERIMENTAL METHODS

Polycrystalline samples of XPd_2Sn ($X = \text{Ti}, \text{Zr}, \text{Hf}$) were prepared by arc-melting the pure metals under an argon atmosphere. The samples were sealed in evacuated quartz tubes and annealed at 850 °C for two weeks to ensure homogeneity. The crystal structures were characterized by powder x-ray diffraction (XRD) on a PANalytical X'Pert MRD diffractometer with $\text{Cu K}\alpha$ radiation, including low temperature measurements down to 30 K. The electrical transport and specific heat measurements were performed on a Physical Property Measurement System (PPMS, Quantum Design) with a ^3He insert. The magnetization was measured using a SQUID magnetometer (MPMS-5T, Quantum Design). Single crystal XRD measurements were performed down to 90 K using a Bruker D8 Venture diffractometer. Tiny single crystals were selected from surface of the polycrystalline samples. The reciprocal space reconstruction of the single-crystal XRD data was performed using the APEX4 software. The electronic structure and density of states (DOS) of XPd_2Sn ($X = \text{Ti}, \text{Zr}, \text{Hf}$) were calculated using density functional theory (DFT) as implemented in VASP [33, 34]. The Perdew-Burke-Ernzerhoff (PBE) flavor of the generalized gradient approximation was employed, where the energy cutoff was chosen to be 400 eV and the Brillouin zone was sampled with $12 \times 12 \times 12$ Γ -centered k -mesh. Spin-orbit coupling was taken into account using a second variation method. The first-principles results were fitted to a tight-binding model Hamiltonian using maximally projected Wannier functions (MLWF) to calculate the static bare electron susceptibility [35, 36]. The phonon dispersion was calculated using density functional perturbation theory (DFPT) as implemented in the Quantum ESPRESSO package [37]. The DFPT calculations were performed using Troullier-Martins norm-conserving pseudopotentials, with an energy cut-off of 144 Ry and $6 \times 6 \times 6$ q -mesh.

III. RESULTS

A. Structural phase transitions

Powder XRD patterns of XPd_2Sn ($X = \text{Ti}, \text{Zr}$ and Hf) measured at 300 K are shown in Fig. 1. The patterns exhibit broadened Bragg peaks, which may be

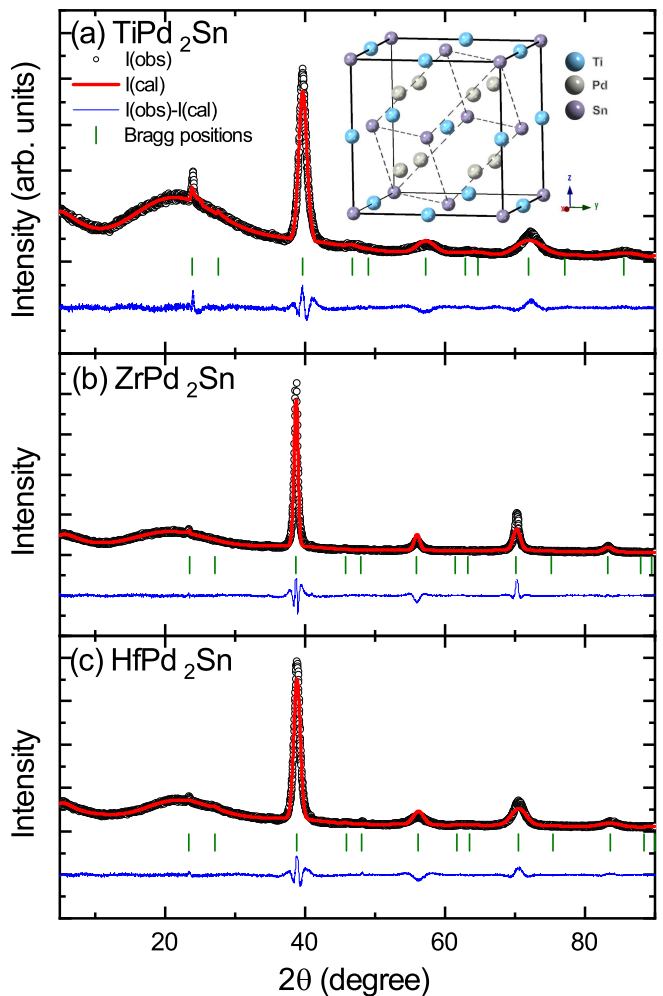


FIG. 1. (Color online) Room-temperature powder x-ray diffraction patterns of polycrystalline (a) TiPd_2Sn (b) ZrPd_2Sn and (c) HfPd_2Sn . The open symbols represent the observed data, the red solid lines denote the calculated patterns from the Rietveld refinements and the blue solid lines are the differences between the measured and calculated results. The green vertical lines denote the expected Bragg peak positions. Inset of (a): Crystal structure of TiPd_2Sn at room temperature. The dashed lines denote the primitive unit cell.

due to the small size of the crystalline grains or a reduced crystallinity. The full width at half maximum (FWHM) values of the main (220) peak are 1.25° , 0.78° and 0.91° for TiPd_2Sn , ZrPd_2Sn and HfPd_2Sn , respectively. All the diffraction peaks can be well indexed to the cubic MnCu_2Al -type structure with space group $Fm\bar{3}m$. Rietveld refinements yield lattice parameters of $a = 6.3351(3)$ Å, $6.5608(2)$ Å and $6.5272(3)$ Å for TiPd_2Sn , ZrPd_2Sn and HfPd_2Sn , respectively, which are close to the previously reported values [38]. The crystal structure of TiPd_2Sn is shown in the inset of Fig. 1(a). The Ti-Pd atoms form a NaCl-type sublattice while Pd atoms fill the tetrahedral voids.

Figure 2 shows the temperature dependence of the elec-

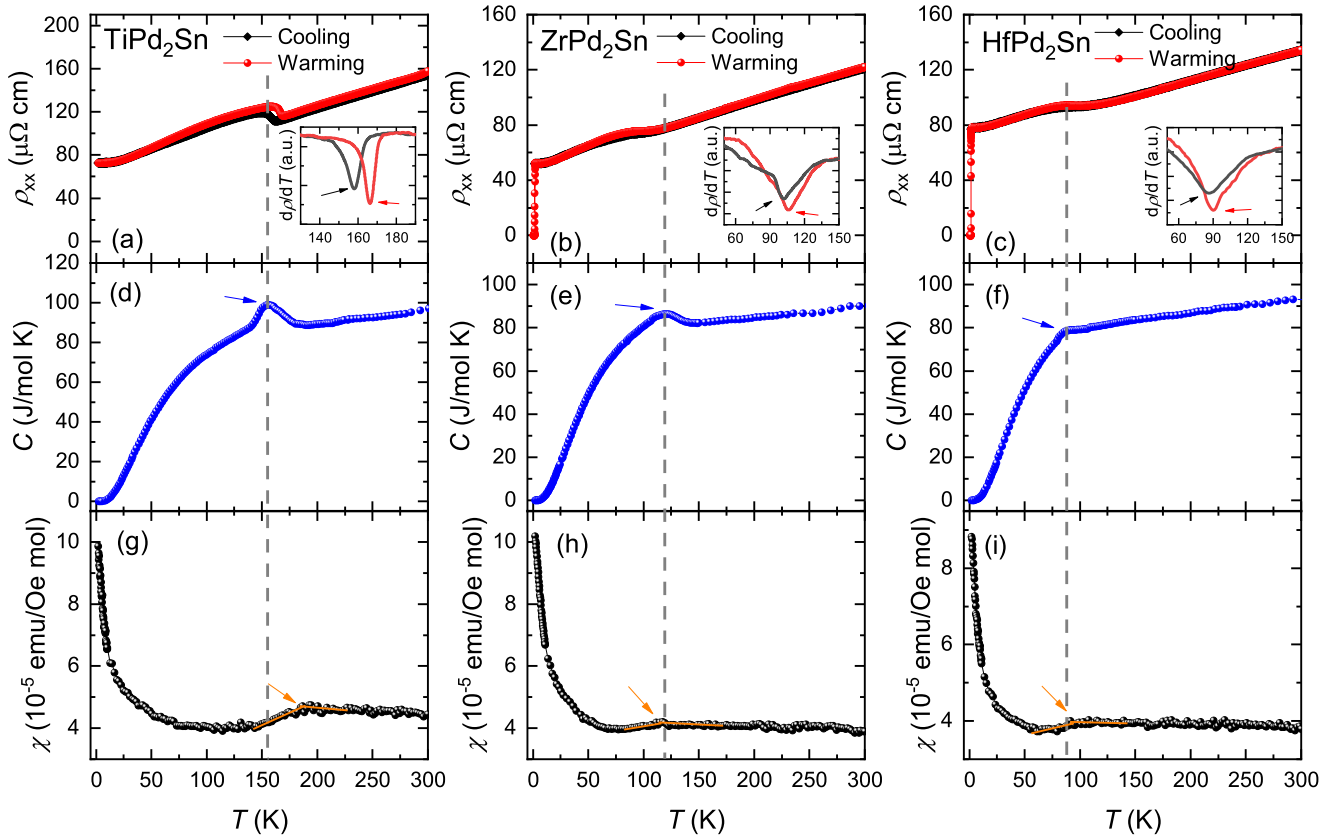


FIG. 2. (Color online) Temperature dependence of (a), (b) and (c): electrical resistivity $\rho_{xx}(T)$ measured upon warming and cooling, (d), (e) and (f): specific heat $C(T)$ and (g), (h) and (i): magnetic susceptibility $\chi(T)$ for TiPd_2Sn , ZrPd_2Sn and HfPd_2Sn , respectively. The $C(T)$ and $\chi(T)$ data are measured upon warming. The insets show the derivative of $\rho_{xx}(T)$ near T_s . The arrows in all the panels denote the structural transitions (see text), corresponding to the values in Table I. The vertical dashed lines correspond to the structural transition temperatures from the specific heat, which are shown as guides to the eye.

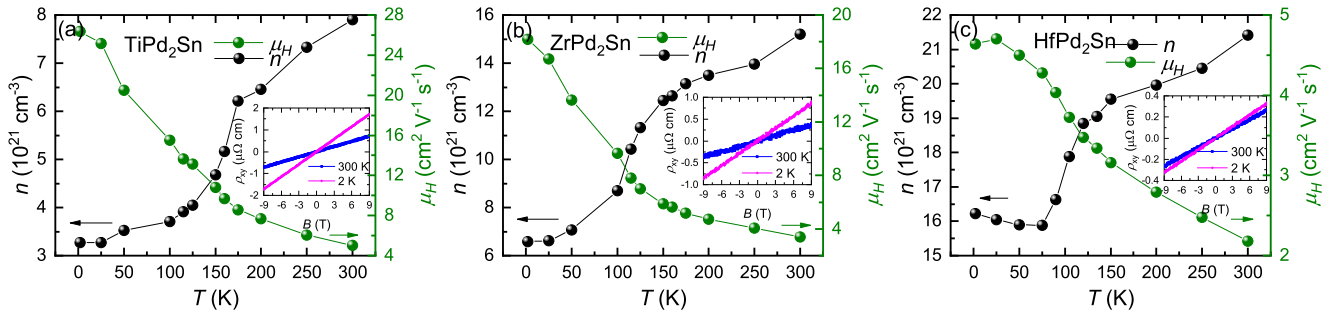


FIG. 3. (Color online) The temperature dependence of the carrier density and mobility of the Hall resistivity of (a) TiPd_2Sn , (b) ZrPd_2Sn and (c) HfPd_2Sn . The field-dependence of the Hall resistivity at two temperatures are shown in the insets.

trical resistivity $\rho_{xx}(T)$, specific heat $C(T)$ and magnetic susceptibility $\chi(T)$ of the three materials, measured from 300 K to 0.5 K. Upon lowering the temperature from 300 K, the decrease of $\rho_{xx}(T)$ indicates a metallic nature. The $\rho_{xx}(T)$ of TiPd_2Sn exhibits a jump at around 160 K with clear hysteresis between the measurements performed upon cooling down and warming up, indicating a first-order transition. In the case of ZrPd_2Sn and HfPd_2Sn , pronounced humps and moderate hysteresis

are also observed, at around 110 K and 90 K, respectively. The increase of the resistivity below T_s could be due to the opening of a partial gap on the Fermi surface associated with the formation of CDW order. In addition, $C(T)$ shown in Figs. 2(d), (e) and (f) have δ -like anomalies at T_s , with relatively broad transition widths. The temperature dependence of the magnetic susceptibility $\chi(T)$ was measured in an applied field of 4 T (Figs. 2(g), (h) and (i)). Below T_s , there is a slight but observ-

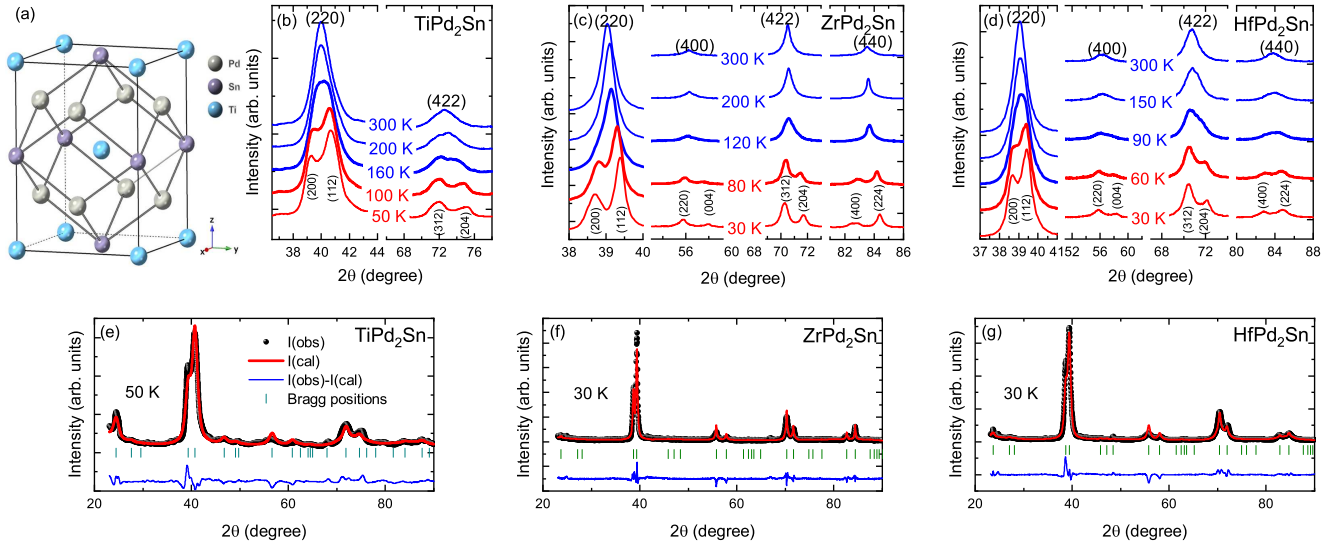


FIG. 4. (Color online) (a) Low temperature tetragonal crystal structure of TiPd_2Sn . (b), (c) and (d): powder x-ray diffraction patterns of XPd_2Sn ($X = \text{Ti}, \text{Zr}, \text{Hf}$) measured at various temperatures, focusing on a few major diffraction peaks. The corresponding powder x-ray diffraction patterns together with the calculated results from Rietveld refinements at the lowest measured temperatures ($T < T_s$) are shown in (e), (f) and (g).

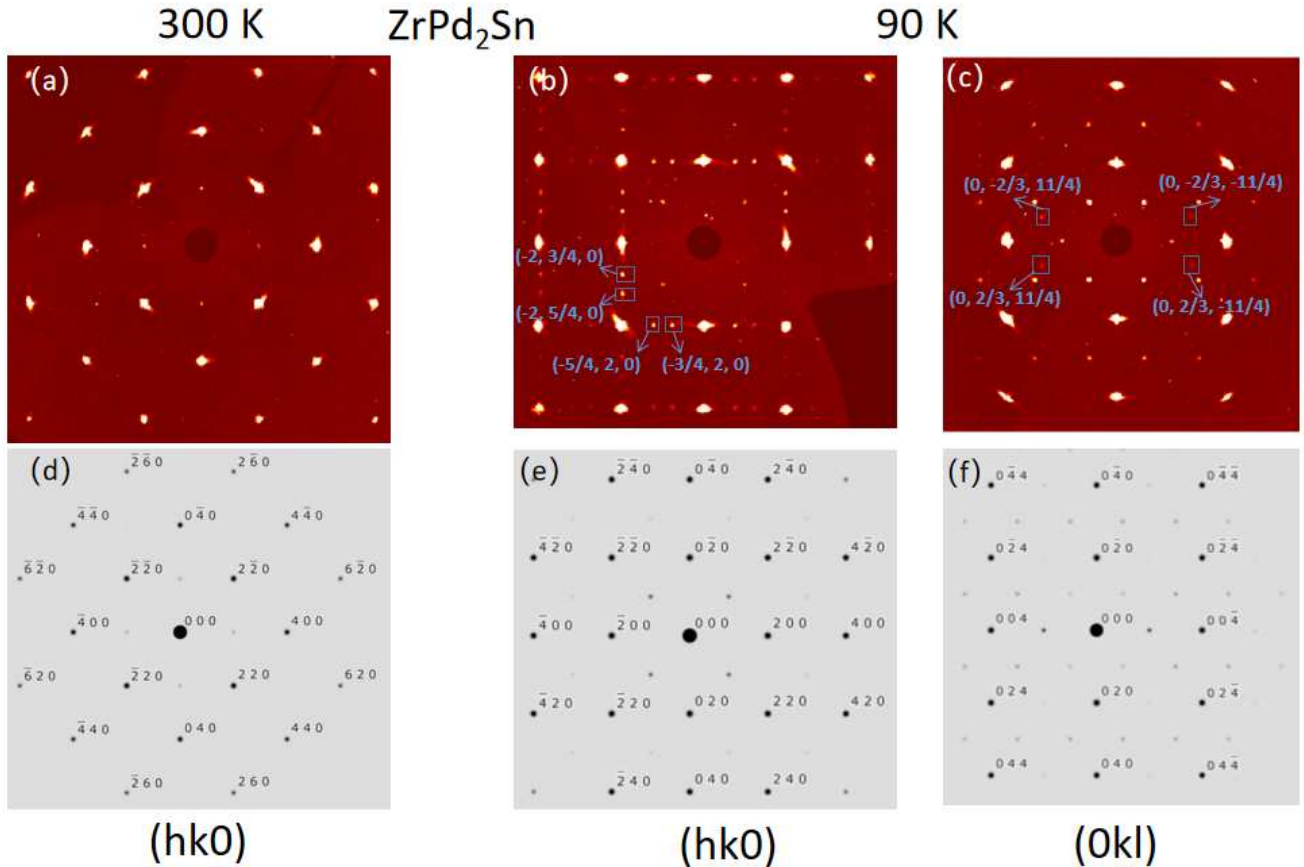


FIG. 5. (Color online) Single-crystal XRD results for ZrPd_2Sn . Reciprocal space images are shown for (a) the $(hk0)$ plane at 300 K ($T > T_s$), (b) $(hk0)$ and (c) $(0kl)$ at 90 K ($T < T_s$). (d) Simulated diffraction pattern in the $(hk0)$ plane for the cubic crystal structure (space group $Fm\bar{3}m$.) (e) and (f) Simulated diffraction pattern in the $(hk0)$ and $(0kl)$ planes for the low temperature tetragonal crystal structure (space group $I4/mmm$.) Representative additional low temperature satellite peaks in (b) and (c) are also labelled.

able drop in $\chi(T)$, in line with a decrease of the density of states at the Fermi level. We define the resistivity transition temperature T_s as where the derivative of the $\rho_{xx}(T)$ reaches a minimum (insets of Figs. 2(a)-(c)). The corresponding values of T_s from the specific data are determined from the peak maximum or turning point, while for the magnetic susceptibility it corresponds to the onset of the decrease. It can be clearly seen that in all three compounds, the T_s determined from $\rho_{xx}(T)$, $C(T)$, and $\chi(T)$ are close, as shown in Table. I, and do not appear to depend on the applied field.

The Hall resistivity ρ_{xy} was measured at various temperatures from 300 K to 2 K as a function of applied magnetic field up to 9 T, as shown for two temperatures in the insets of Fig. 3. The almost linear dependence of $\rho_{xy}(B)$ within the measured field range and the positive slope suggest that hole-type carriers are dominant for all three compounds. The carrier concentration n and Hall mobility μ_H can be deduced from a one-band model and their temperature dependences are shown in Fig. 3. Here n was determined from the Hall coefficient $R_H = 1/ne$, where R_H is derived from the slope of ρ_{xy} , while μ_H was determined from $\mu_H = 1/(ne\rho_{xx})$, where ρ_{xx} is the resistivity data from Fig. 2. For all three compounds, the carrier concentrations have step-like drops with decreasing temperature, very close to where the anomalies are observed in $\rho_{xx}(T)$, $C(T)$ and $\chi(T)$, and this reduction may be due to the partial opening of a gap. The Hall mobility μ_H increases as the temperature decreases, with an observable anomaly near T_s . From TiPd₂Sn to ZrPd₂Sn and HfPd₂Sn, the overall value of n increases, while μ_H decreases.

Powder XRD measurements were performed at various temperatures below 300 K to investigate the evolution of the structure below T_s . Upon cooling below T_s , clear splitting of the major diffraction peaks can be resolved, as shown in Fig. 4. These indicate that XPd₂Sn ($X = \text{Ti, Zr, Hf}$) undergo a structural transition across T_s , which is consistent with the first-order characteristics shown in the resistivity and specific heat. For all three materials, the patterns below T_s can be well indexed by a tetragonal structure (space group $I4/mmm$). Rietveld refinements of the XRD data measured at the lowest temperatures were performed based on the tetragonal structure with space group $I4/mmm$ shown in Fig. 4(a) [14, 39], where the X, Pd, and Sn are situated at the $2a$, $4d$, and $2b$ Wyckoff positions, respectively. The calculated patterns are shown in Figs. 4(e)-(g), where there is good agreement of the data with the tetragonal model for all three compounds, and the fitted lattice parameters are displayed in Table. I. It is noted that structural transitions have been reported in a few RE T_2X compounds with the Heusler structure, such as (Yb, Lu)Pt₂In [30, 31] and REAu₂In (RE = La-Nd) [32].

To further investigate the nature of structural phase transition, we performed single-crystal XRD measure-

ments on the tiny single crystals selected from the surface of the arc-melted samples. We successfully obtained clear single crystal XRD data for ZrPd₂Sn (shown in Fig. 5 (a)-(c)), where the smaller FWHM in the powder XRD patterns suggests a higher degree of crystallinity compared to the other two compounds. In Fig. 5(d), the simulated patterns are shown for the cubic MnCu₂Al-type structure (space group $Fm\bar{3}m$), which are consistent with the experimental results at 300 K displayed in Fig. 5(a). At 90 K, the main reflections are well indexed by a tetragonal structure with space group $I4/mmm$, confirming the change from cubic to tetragonal symmetry upon cooling through T_s . Furthermore, at 90 K, additional peaks are observed experimentally corresponding to non-integer (hkl), as labelled in Figs. 5(b) and (c), indicating the formation of a superlattice structure. From the measurements in the ($hk0$) plane (Fig. 5(b)), peaks such as $(-2, 3/4, 0)$ and $(-2, 5/4, 0)$ are observed, which correspond to a commensurate modulation vector of $(3/4, 0, 0)$. While in Fig. 5(c), there are further additional peaks such as $(0, 2/3, 11/4)$, pointing to there being multiple commensurate structural modulations below T_s . The appearance of a superlattice structure with multiple commensurate structural modulations below T_s in ZrPd₂Sn suggests the onset of CDW order below the structural transition.

B. Superconductivity

Figure 6 displays the low temperature $\rho_{xx}(T)$, $\chi(T)$ and electronic specific heat $C_e(T)/T$ of ZrPd₂Sn and HfPd₂Sn. The resistivity $\rho_{xx}(T)$ shows sharp superconducting transitions where ρ_{xx} reaches zero at around 1.2 K and 1.4 K for ZrPd₂Sn and HfPd₂Sn, respectively. The temperature dependence of $\chi(T)$ was measured under an applied magnetic field of 1 mT after zero-field cooling (ZFC) and field cooling (FC) processes. Clear diamagnetic signals are observed in the ZFC curves close to where $\rho_{xx}(T)$ reaches zero and the saturated values of $4\pi\chi$ are close to -1, which correspond to full diamagnetic shielding. The significant difference between ZFC and FC curves can be due to the magnetic flux pinning between grains. The electronic specific heat $C_e(T)/T$ are shown in Figs. 6(e) and (f), after subtracting the phonon contribution βT^3 , where $C_p(T) = \gamma_n T + \beta T^3$ in the normal state, as shown in the insets. The fitted parameters are $\gamma_n = 4.77(1)$ and $4.72(4)$ mJ mol⁻¹ K⁻², $\beta = 1.02(1)$ and $1.55(1)$ mJ mol⁻¹ K⁻⁴ for ZrPd₂Sn and HfPd₂Sn, respectively. The low γ_n values suggest weak electronic correlations. The Debye temperatures θ_D are estimated to be 197 K and 171 K, respectively, using $\theta_D = (12nR\pi^4/5\beta)^{1/3}$ with $n = 4$ (number of atoms per formula unit) and $R = 8.314$ J mol⁻¹ K⁻¹ (molar gas constant). The jump of C_e/T at T_c indicates bulk superconductivity, where the normalized jump values $\Delta C/\gamma_n T_c$

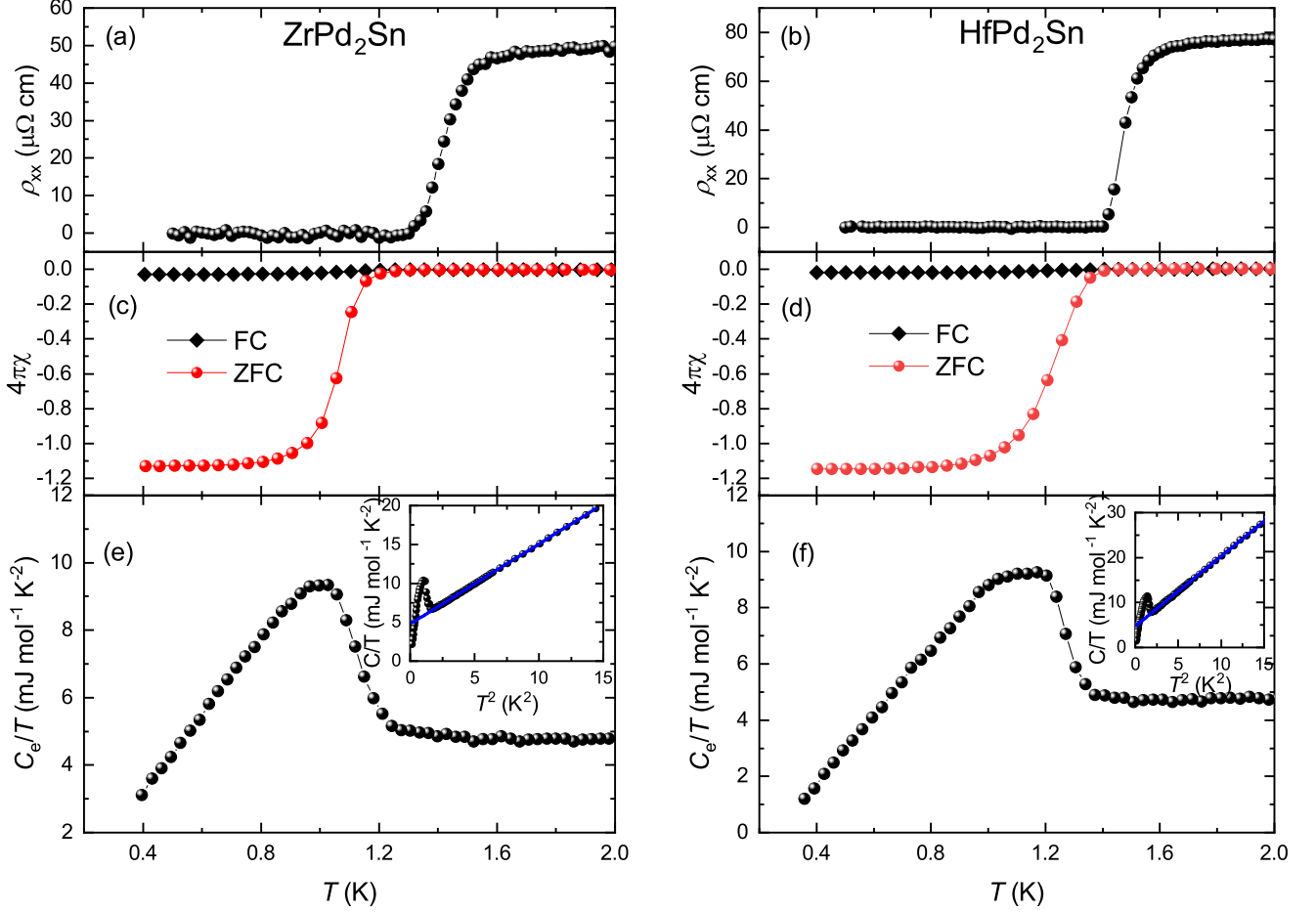


FIG. 6. (Color online) The temperature dependence of (a), (b): electrical resistivity and (c), (d): magnetic susceptibility and (e), (f): electronic specific heat of ZrPd_2Sn and HfPd_2Sn near the superconducting transition T_c . Insets of (e) and (f) show the total specific heat $C(T)/T$ vs T^2 , where solid lines denote fits of the phonon contribution.

are 1.1 and 1.2 for the respective materials. The electron-phonon coupling constant λ_{ep} is related to T_c and θ_D and can be estimated using the McMillan formula

$$\lambda_{ep} = \frac{1.04 + \mu^* \ln(\theta_D/1.45T_c)}{(1 - 0.62\mu^*) \ln(\theta_D/1.45T_c) - 1.04} \quad (1)$$

where using a repulsive screened Coulomb parameter μ^* of 0.13 yields λ_{ep} values of 0.49 (ZrPd_2Sn) and 0.52 (HfPd_2Sn), indicating weak electron-phonon coupling.

Figures 7(a) and (b) display the temperature dependence of the electrical resistivity of ZrPd_2Sn and HfPd_2Sn under various applied magnetic fields. The superconducting transitions are shifted to lower temperatures with increasing magnetic field. The temperature dependence of the upper critical field are shown in Figs. 7(a) and (b), where the values of T_c are determined from the midpoint of the resistivity drop at the transition. The data are fitted by the Ginzburg-Landau (G-L) phenomenological model

$$\mu_0 H_{c2}(T) = \mu_0 H_{c2}(0) \frac{1 - (T/T_c)^2}{1 + (T/T_c)^2} \quad (2)$$

which yields $\mu_0 H_{c2}(0) = 0.32(2)$ T for ZrPd_2Sn and $0.43(2)$ T for HfPd_2Sn . The Ginzburg-Landau coherence length ξ_{GL} are calculated to be $32(1)$ nm (ZrPd_2Sn) and $28(1)$ nm (HfPd_2Sn) via $\xi_{GL} = \sqrt{\Phi_0/2\pi\mu_0 H_{c2}(0)}$, where Φ_0 is the magnetic flux quantum.

C. DFT calculations

The electronic band structure and density of states (DOS) of XPd_2Sn ($X = \text{Ti}, \text{Zr}, \text{Hf}$) are shown in Figs. 8(a)-(c), which are consistent with the previous report [40]. The behaviour of the three materials are similar, where two bands crossing the Fermi level indicates a metallic nature. The X -d (Ti-3d, Zr-4d, Hf-5d) and Pd-4d orbitals dominate the DOS within ± 2 eV of the Fermi level while contributions to the DOS from other orbitals are negligible. The static bare electronic susceptibility $\chi_0(q)$ are also calculated, as shown in Figs. 8(d)-(f), and the imaginary parts of χ_0 are obtained by calculating the nesting function. For all the three materials, the real parts of χ_0 show humps in the middle of $K - \Gamma$

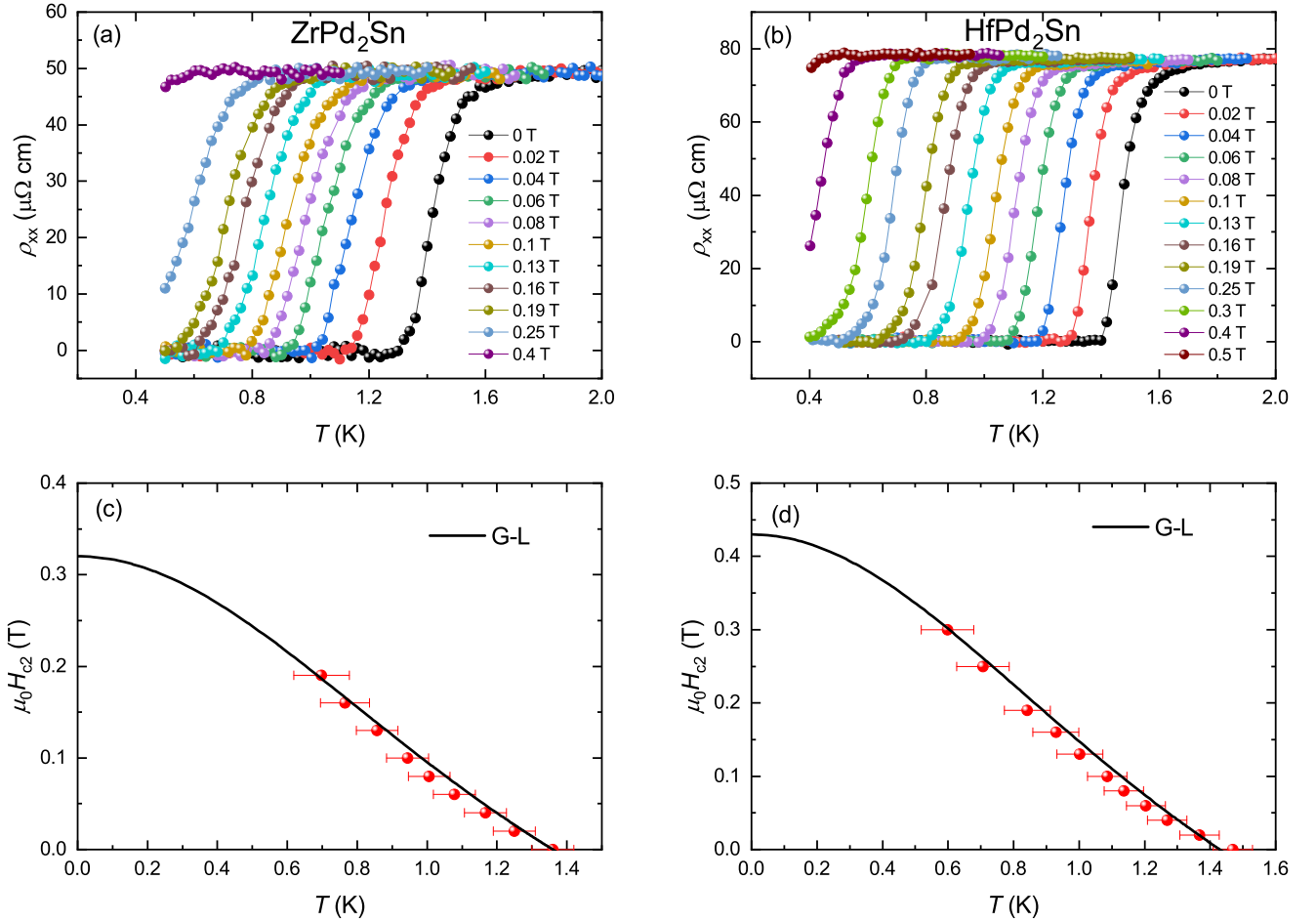


FIG. 7. (Color online) (a), (b): Temperature dependence of the electrical resistivity of ZrPd_2Sn and HfPd_2Sn , measured under various applied magnetic fields in the vicinity of T_c . The upper critical fields $\mu_0 H_{c2}(T)$ are shown in (c) and (d), T_c was determined from the midpoint of the resistivity drop at the transition. The solid lines correspond to fitting using the Ginzburg-Landau (G-L) model.

and $\Gamma - L$, where peaks in the imaginary parts can also be identified. In addition, several smaller nesting function peaks can also be identified around X , K and U , indicating that charge fluctuations are anticipated. Figures 8(g)-(i) show the phonon spectra of XPd_2Sn calculated from first principles using the cubic Heusler structure unit cell. Imaginary phonon modes are found at $q = X$, K and U points in all three cases, corresponding to structural instabilities and suggest the presence of a CDW [41]. Such dynamically unstable crystal structures are consistent with the experimental observations of structural phase transitions. The magnitude of the negative phonon frequencies slightly decreases from TiPd_2Sn to ZrPd_2Sn to HfPd_2Sn , which is consistent with the corresponding decrease in T_s . We note that imaginary phonon modes were also observed in LiPd_2Ge [42] and LuPt_2In [30, 43]. However for LiPd_2Ge , the small imaginary phonon mode appears between Γ and K and leads to superconductivity around 1 K, while for LuPt_2In , the large soft phonon mode corresponds to a very high CDW

transition temperature around 490 K.

IV. DISCUSSION AND SUMMARY

Our experimental measurements indicate that TiPd_2Sn , ZrPd_2Sn and HfPd_2Sn undergo a structural phase transition at $T_s \sim 160 - 90$ K, which potentially corresponds to a CDW instability. We confirm the existence of a superlattice structure in ZrPd_2Sn below T_s , corresponding to multiple commensurate structural modulations, suggesting the formation of CDW order. To further investigate the nature of the structural transition and possible CDW order, additional measurements are required on high quality single crystals such as electron microscopy, and x-ray scattering experiments. It is noted that superconductivity is not found in TiPd_2Sn down to 0.5 K, and this compound also has the largest value of T_s . Meanwhile, ZrPd_2Sn and HfPd_2Sn have comparatively lower values of T_s , and become superconducting below around 1 K. Furthermore, the

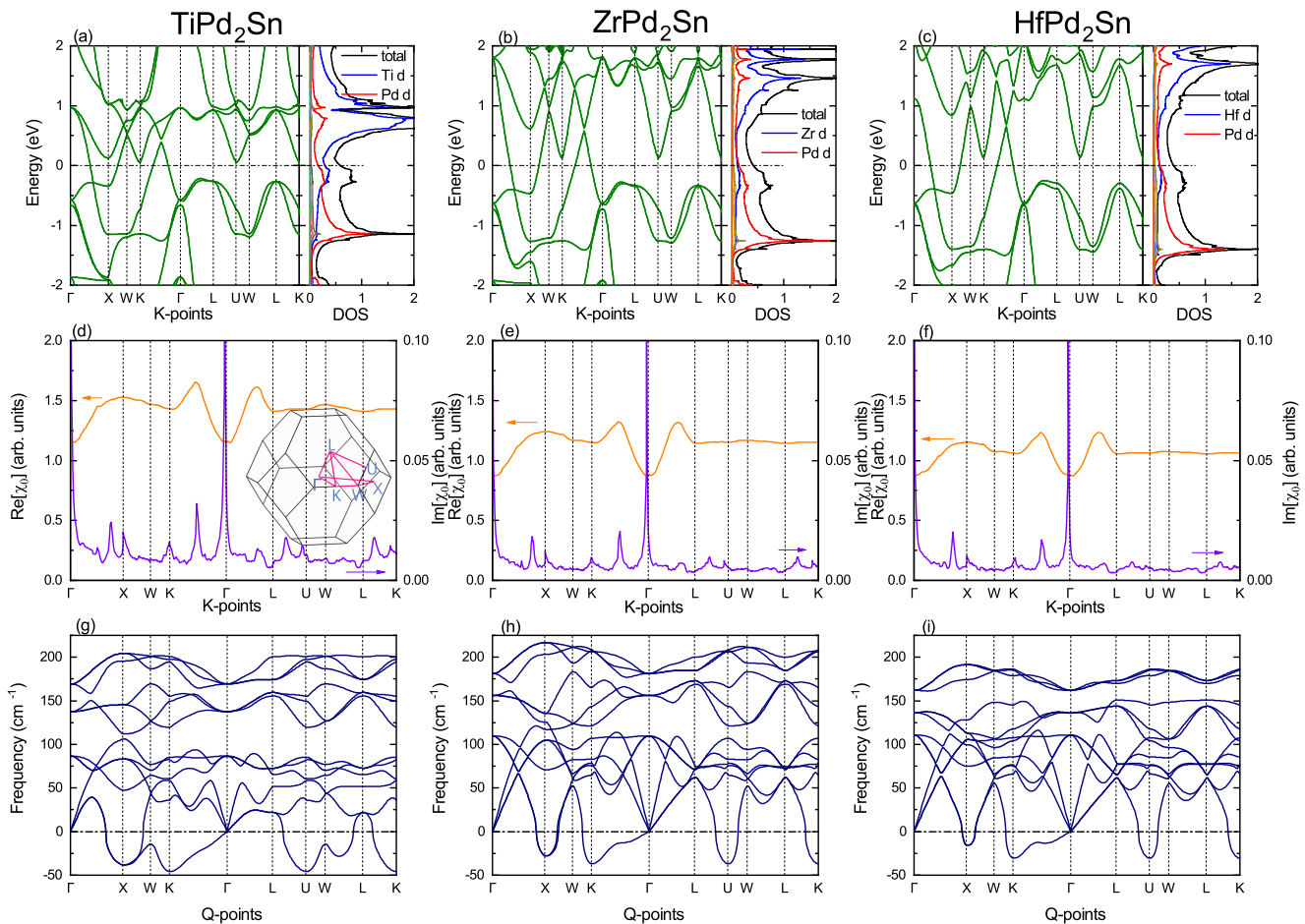


FIG. 8. (Color online) DFT calculations of XPd_2Sn ($X = Ti, Zr, Pd$). (a), (b) and (c): electronic band structure and density of states, taking into account spin-orbit coupling (SOC). (d), (e) and (f): bare electron susceptibility χ_0 , where the orange (purple) solid lines denote real (imaginary) parts. Inset of (d): Brillouin zone and high symmetry points, and (g), (h) and (i): Phonon spectra of the three compounds.

TABLE I. Properties of XPd_2Sn including the structural transition temperatures T_s measured using different techniques, the lattice parameters in the cubic phase at 300 K and in the tetragonal phase at T_{min} , as well as the Debye temperature θ_D , the superconducting transition temperature T_c , and the zero-temperature upper critical field $\mu_0 H_{c2}(0)$.

Parameters	TiPd ₂ Sn	ZrPd ₂ Sn	HfPd ₂ Sn
$T_s^{\rho\uparrow}$ (K)	166	106	90
$T_s^{\rho\downarrow}$ (K)	158	102	86
T_s^C (K)	155	119	88
T_s^X (K)	181	115	95
a (Å) (300 K)	6.3351(3)	6.5608(2)	6.5271(3)
a (Å) (T_{min})	4.5882(7)	4.6622(6)	4.6155(6)
c (Å) (T_{min})	6.0451(6)	6.4012(5)	6.3352(5)
θ_D (K)	237	197	171
T_c (K)	-	1.2	1.3
$\mu_0 H_{c2}(0)$ (T)	-	0.32(2)	0.43(2)

signature of T_s in the resistivity is more pronounced in TiPd₂Sn than in the other two compounds (Fig. 2),

which may reflect the more extensive opening of a gap on the Fermi surface for the former. These indicate possible competition between superconductivity and the CDW/structural phase transition, which has been intensively investigated in other CDW superconductors such as the dichalcogenides [44] and intermetallics (Ca, Sr)₃(Rh, Ir)₄Sn₁₃ [23, 45]. The origin of CDW order is often attributed to electron-phonon coupling or Fermi surface nesting. We note here that while there are peaks in the nesting function around the q -vectors where the imaginary phonon modes appear, these nesting function peaks are not the most prominent ones. Therefore, it is likely that the CDW in these compounds originate from electron-phonon coupling, similar to the case in Lu(Pt, Pd)₂In [43]. Considering that the cubic structure of XPd_2Sn does not have low dimensional characteristics, a three-dimensional CDW is also expected. In addition, the possible existence of a CDW QCP reported in Lu(Pt_{1-x}Pd_x)₂In indicates that the Heusler materials are potential candidates for investigating CDW-related quantum criticality. However, different from the

second-order CDW transition in LuPt₂In, the first-order structural phase transitions observed here in XPd₂Sn points to the absence of quantum phase transitions or quantum criticality. On the other hand, chemical substitution and hydrostatic pressure can potentially be used to tune the structural phase transitions and superconductivity, which may provide insights into their interplay.

In summary, we have synthesized polycrystalline samples of XPd₂Sn ($X = \text{Ti, Zr, Hf}$) and studied their structural and physical properties. Structural phase transitions from the high temperature cubic MnCu₂Al-type structure ($Fm\bar{3}m$) to a low-temperature tetragonal structure, are observed in the three materials, at respective temperatures of around $T_s \sim 160, 110, \text{ and } 90 \text{ K}$. Low temperature single-crystal XRD measurements of ZrPd₂Sn show the presence of a superlattice structure below T_s , with multiple commensurate modulations, providing evidence for the formation of CDW order. Bulk superconductivity in ZrPd₂Sn and HfPd₂Sn is observed with respective transition temperatures $T_c = 1.2 \text{ and } 1.3 \text{ K}$. DFT calculations show the presence of imaginary phonon modes that suggest a structural instability driven by electron-phonon coupling, together with humps in Fermi surface nesting functions. These findings suggest that XPd₂Sn are promising systems for examining the interplay of superconductivity and CDW order.

ACKNOWLEDGMENTS

We thank G. Cao, Y. Liu and S. Song for assisting with x-ray diffraction and ³He-SQUID measurements. This work was supported by the Key R&D Program of Zhejiang Province, China (2021C01002), the National Natural Science Foundation of China (Grants No. 11874320, No. 11974306, No. 12034017, and No. 11874137), the Zhejiang Provincial Natural Science Foundation of China (R22A0410240), and the National Key R&D Program of China (Grant No. 2017YFA0303100).

* Corresponding author: mmsmidman@zju.edu.cn

† Corresponding author: hqyuan@zju.edu.cn

- [1] F. Heusler, *Verhandlungen der Deutschen Physikalischen Gesellschaft* **5**, 219 (1903).
- [2] J. Dshemuchadse and W. Steurer, *Acta Cryst. A* **71**, 335 (2015).
- [3] R. Pöttgen and D. Johrendt, *Intermetallics* (de Gruyter, 2019).
- [4] S. Takayanagi, S. Woods, N. Wada, T. Watanabe, Y. Ōnuki, A. Kobori, T. Komatsubara, M. Imai, and H. Asano, *J. of Magn. and Magn. Mater.* **76-77**, 281 (1988).
- [5] K. Gofryk, D. Kaczorowski, and A. Czopnik, *Solid State Commun.* **133**, 625 (2005).
- [6] Z. H. Liu, M. Zhang, Y. T. Cui, Y. Q. Zhou, W. H. Wang, G. H. Wu, X. X. Zhang, and G. Xiao, *Appl. Phys. Lett.* **82**, 424 (2003).
- [7] P.-J. Guo, H.-C. Yang, K. Liu, and Z.-Y. Lu, *Phys. Rev. B* **95**, 155112 (2017).
- [8] X.-Q. Chen, R. Podloucky, and P. Rogl, *J. Appl. Phys.* **100**, 113901 (2006).
- [9] N. Kourov, V. Marchenkov, A. Korolev, L. Stashkova, S. Emel'yanova, and H. Weber, *Phys. Solid State* **57**, 700 (2015).
- [10] R. Shan, H. Sukegawa, W. H. Wang, M. Kodzuka, T. Furubayashi, T. Ohkubo, S. Mitani, K. Inomata, and K. Hono, *Phys. Rev. Lett.* **102**, 246601 (2009).
- [11] L. Wollmann, A. K. Nayak, S. S. Parkin, and C. Felser, *Annu. Rev. Mater. Res.* **47**, 247 (2017).
- [12] V. Alijani, J. Winterlik, G. H. Fecher, and C. Felser, *Appl. Phys. Lett.* **99**, 222510 (2011).
- [13] T. Graf, C. Felser, and S. S. Parkin, *Prog. Solid State Chem.* **39**, 1 (2011).
- [14] J. Suits, *Solid State Commun.* **18**, 423 (1976).
- [15] J. Wernick, G. Hull, T. Geballe, J. Bernardini, and J. Waszczak, *Mater. Lett.* **2**, 90 (1983).
- [16] R. N. Shelton, L. S. Hausermann-Berg, M. J. Johnson, P. Klavins, and H. D. Yang, *Phys. Rev. B* **34**, 199 (1986).
- [17] T. Klimczuk, C. H. Wang, K. Gofryk, F. Ronning, J. Winterlik, G. H. Fecher, J.-C. Griveau, E. Colineau, C. Felser, J. D. Thompson, D. J. Safarik, and R. J. Cava, *Phys. Rev. B* **85**, 174505 (2012).
- [18] W. L. McMillan, *Phys. Rev. B* **14**, 1496 (1976).
- [19] A. Gabovich, A. Voitenko, and M. Ausloos, *Phys. Rep.* **367**, 583 (2002).
- [20] G. Grüner, *Rev. Mod. Phys.* **60**, 1129 (1988).
- [21] C.-W. Chen, J. Choe, and E. Morosan, *Rep. Prog. Phys.* **79**, 084505 (2016).
- [22] A. F. Kusmartseva, B. Sipos, H. Berger, L. Forró, and E. Tutiš, *Phys. Rev. Lett.* **103**, 236401 (2009).
- [23] L. E. Klintberg, S. K. Goh, P. L. Alireza, P. J. Saines, D. A. Tompsett, P. W. Logg, J. Yang, B. Chen, K. Yoshimura, and F. M. Grosche, *Phys. Rev. Lett.* **109**, 237008 (2012).
- [24] B. R. Ortiz, L. C. Gomes, J. R. Morey, M. Winiarski, M. Bordelon, J. S. Mangum, I. W. H. Oswald, J. A. Rodriguez-Rivera, J. R. Neilson, S. D. Wilson, E. Ertekin, T. M. McQueen, and E. S. Toberer, *Phys. Rev. Materials* **3**, 094407 (2019).
- [25] B. R. Ortiz, S. M. L. Teicher, Y. Hu, J. L. Zuo, P. M. Sarte, E. C. Schueller, A. M. M. Abeykoon, M. J. Krogstad, S. Rosenkranz, R. Osborn, R. Seshadri, L. Balents, J. He, and S. D. Wilson, *Phys. Rev. Lett.* **125**, 247002 (2020).
- [26] F. Du, S. Luo, B. R. Ortiz, Y. Chen, W. Duan, D. Zhang, X. Lu, S. D. Wilson, Y. Song, and H. Yuan, *Phys. Rev. B* **103**, L220504 (2021).
- [27] F. Du, S. S. Luo, R. Li, B. R. Ortiz, Y. Chen, S. D. Wilson, Y. Song, and H. Q. Yuan, *Chinese Phys. B* (2021).
- [28] B. Shen, F. Du, R. Li, A. Thamizhavel, M. Smidman, Z. Y. Nie, S. S. Luo, T. Le, Z. Hossain, and H. Q. Yuan, *Phys. Rev. B* **101**, 144501 (2020).
- [29] F. Du, H. Su, S. S. Luo, B. Shen, Z. Y. Nie, L. C. Yin, Y. Chen, R. Li, M. Smidman, and H. Q. Yuan, *Phys. Rev. B* **102**, 144510 (2020).
- [30] T. Gruner, D. Jang, Z. Huesges, R. Cardoso-Gil, G. H. Fecher, M. M. Koza, O. Stockert, A. P. Mackenzie, M. Brando, and C. Geibel, *Nat. Phys.* **13**, 967 (2017).

- [31] T. Gruner, D. Jang, A. Steppke, M. Brando, F. Ritter, C. Krellner, and C. Geibel, *J. Phys.: Condens. Matter* **26**, 485002 (2014).
- [32] M. Besnus, J. Kappler, M. Ravet, A. Meyer, R. Lahiouel, J. Pierre, E. Siaud, G. Nieva, and J. Sereni, *J. Less-Common Met.* **120**, 101 (1986).
- [33] G. Kresse and J. Hafner, *Phys. Rev. B* **47**, 558 (1993).
- [34] G. Kresse and D. Joubert, *Phys. Rev. B* **59**, 1758 (1999).
- [35] I. Souza, N. Marzari, and D. Vanderbilt, *Phys. Rev. B* **65**, 035109 (2001).
- [36] A. A. Mostofi, J. R. Yates, Y.-S. Lee, I. Souza, D. Vanderbilt, and N. Marzari, *Comput. Phys. Commun.* **178**, 685 (2008).
- [37] P. Giannozzi, S. Baroni, N. Bonini, M. Calandra, R. Car, C. Cavazzoni, D. Ceresoli, G. L. Chiarotti, M. Cococcioni, I. Dabo, A. D. Corso, S. de Gironcoli, S. Fabris, G. Fratesi, R. Gebauer, U. Gerstmann, C. Gougoussis, A. Kokalj, M. Lazzeri, L. Martin-Samos, N. Marzari, F. Mauri, R. Mazzarello, S. Paolini, A. Pasquarello, L. Paulatto, C. Sbraccia, S. Scandolo, G. Sclauzero, A. P. Seitsonen, A. Smogunov, P. Umari, and R. M. Wentzcovitch, *J. Phys.: Condens. Matter* **21**, 395502 (2009).
- [38] M. Yin and P. Nash, *Intermetallics* **58**, 15 (2015).
- [39] M. Yin and P. Nash, *J. Alloys Compd.* **650**, 925 (2015).
- [40] M. Wakeel, G. Murtaza, H. Ullah, S. Khan, A. Laref, Z. Ameer, and S. A. Khan, *Physica B* **608**, 412716 (2021).
- [41] H. Chen, X. Xu, C. Cao, and J. Dai, *Phys. Rev. B* **86**, 125116 (2012).
- [42] K. Górnicka, G. Kuderowicz, E. M. Carnicom, K. Kutorasiński, B. Wiendlocha, R. J. Cava, and T. Klimczuk, *Phys. Rev. B* **102**, 024507 (2020).
- [43] H. Kim, B. I. Min, and K. Kim, *Phys. Rev. B* **98**, 144305 (2018).
- [44] A. M. Gabovich, A. I. Voitenko, J. F. Annett, and M. Ausloos, *Supercond. Sci. Technol.* **14**, R1 (2001).
- [45] S. K. Goh, D. A. Tompsett, P. J. Saines, H. C. Chang, T. Matsumoto, M. Imai, K. Yoshimura, and F. M. Grosche, *Phys. Rev. Lett.* **114**, 097002 (2015).